

Constraints on fault and lithosphere rheology from the coseismic slip and postseismic afterslip of the 2006 M_w 7.0 Mozambique earthquake

Alex Copley,¹ James Hollingsworth,² and Eric Bergman³

Received 8 June 2011; revised 13 January 2012; accepted 17 January 2012; published 10 March 2012.

[1] The 2006 M_w 7.0 Mozambique (Machaze) normal-faulting earthquake ruptured an unusually steeply dipping fault plane ($\sim 75^\circ$). The amount of slip in the earthquake decreased from depths of ~ 10 km toward the surface, and this shallow slip deficit was at least partly recovered by postseismic afterslip on the shallow part of the fault plane. An adjacent normal fault segment slipped postseismically (and possibly also co-seismically) at shallow depths with a large strike-slip component, in response to the stresses generated by slip on the main earthquake fault plane. Our observations suggest that the fault zone behaves in a stick-slip manner in the crystalline basement, and that where it cuts the sedimentary layer the coseismic rupture was partially arrested and there was significant postseismic creep. We discuss the effects of such behavior on the large-scale tectonics of continental regions, and on the assessment of seismic hazard on similar fault systems. The steep dip of the fault suggests the re-activation of a preexisting structure with a coefficient of friction at least ~ 25 – 45% lower than that on optimally oriented planes, and analysis of the deformation following an aftershock indicates that the value of the parameter ‘ a ’ that describes the rate-dependence of fault friction lies in the range 1×10^{-3} – 2×10^{-2} . The lack of long-wavelength postseismic relaxation suggests viscosities in the ductile lithosphere of greater than $\sim 2 \times 10^{19}$ Pa s, and an examination of the tectonic geomorphology in the region identifies ways in which similar fault systems can be identified before they rupture in future earthquakes.

Citation: Copley, A., J. Hollingsworth, and E. Bergman (2012), Constraints on fault and lithosphere rheology from the coseismic slip and postseismic afterslip of the 2006 M_w 7.0 Mozambique earthquake, *J. Geophys. Res.*, 117, B03404, doi:10.1029/2011JB008580.

1. Introduction

[2] The M_w 7.0 Mozambique (Machaze) earthquake occurred on 22nd February 2006. Focal mechanisms show the event to be normal faulting at the southern end of the East African Rift system (Figure 1). The Nubia-Somalia Euler pole, which describes the extension occurring on the East African Rift system, lies close to the southern tip of Africa [e.g., *Nocquet et al.*, 2006]. The Mozambique earthquake occurred at latitudes where the rate of extension across the entire plate boundary is ~ 2.5 mm/yr [*Nocquet et al.*, 2006], and the deformation becomes more laterally distributed than in the rift systems further north. One reason for choosing to study this earthquake is that it provides a rare opportunity to study a large earthquake in a region of

slow deformation, and as such provides an interesting comparison with the more common earthquakes from rapidly deforming areas. Additionally, the large volumes of space-based geodetic data available for the region present an opportunity to use the earthquake to probe the rheology of the brittle and ductile portions of the lithosphere. This particular aim is especially timely because of the vigorous current debate regarding the rheology of the continental lithosphere [e.g., *Chen and Molnar*, 1983; *Townend and Zoback*, 2000; *Watts and Burov*, 2003; *Hetenyi et al.*, 2006; *Jackson et al.*, 2008]. Much of the discussion revolves around the magnitude of the stresses that are transmitted through the seismogenic layer compared with the ductile lithosphere. It is therefore worthwhile to attempt to use earthquakes and their postseismic deformation to constrain the rheology of active faults and the ductile lithosphere.

[3] The 2006 Mozambique earthquake occurred on the coastal plain of southern Mozambique (Figure 1), where the surface geology is characterized by quaternary to Neogene sediments [*Salman and Abdula*, 1995]. The sedimentary sequence is 5–10 km thick, and is composed of terrestrial and shallow marine sediments deposited almost continuously since the Jurassic [*Salman and Abdula*, 1995; *Watts*,

¹COMET+, Bullard Labs, Department of Earth Sciences, University of Cambridge, Cambridge, UK.

²Tectonics Observatory, Division of Geological and Planetary Sciences, California Institute of Technology, Pasadena, California, USA.

³Global Seismological Services, Golden, Colorado, USA.

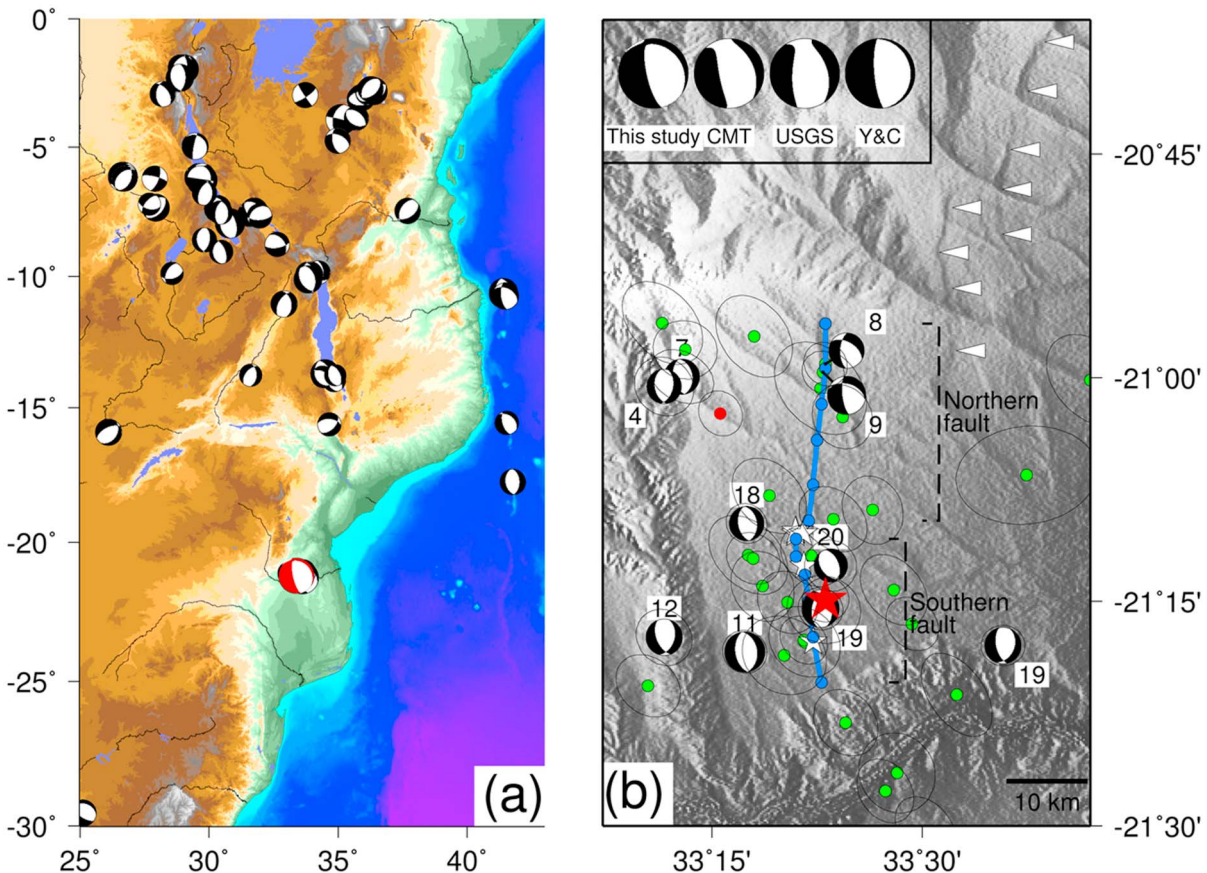


Figure 1. (a) Earthquakes in east Africa [Craig *et al.*, 2011, and references therein]. The 2006 Mozambique main shock is shown in red. (b) Epicentral region of the 2006 Mozambique event, with topography illuminated from the east. The green circles show relocated aftershocks, along with the 90% location confidence ellipses, and the red circle is the aftershock visible in the postseismic InSAR data (section 3). The red star shows the relocated main shock hypocenter. The small focal mechanisms show the aftershocks large enough for source parameters to be obtained ([Yang and Chen, 2008; Craig *et al.*, 2011] and CMT solutions) plotted at the relocated positions and labeled with the depth in kilometers. The blue lines show the fault locations visible in the postseismic InSAR data (section 3), and the blue circles show points along these faults that have been plotted in Figures 2, 5, and 6 to indicate the locations. The white stars show the locations of Fenton and Bommer's [2006] observations of surface faulting, and the white arrows in the northeast show the locations of fault scarps visible in the geomorphology. Also shown is a comparison of focal mechanisms for the main shock (Y&C: Yang and Chen [2008]).

2001]. Elevations at close to sea level from dates before the breakup of Gondwana, and the presence of pre-breakup to syn-breakup Karoo volcanics, suggest that the coastal plain is underlain by continental crust. Salman and Abdula [1995] suggest that this continental crust is Precambrian in age, and the low elevation compared with the surrounding continental regions possibly indicates that it was slightly thinned during the breakup of Gondwana. To the north and west, the higher ground of the African continental interior is composed of Precambrian continental material with a large lithospheric thickness (up to ~ 200 km [Craig *et al.*, 2011]). The 2006 Mozambique earthquake occurred on the NW side of the coastal plain, ~ 150 km from the exposed Precambrian rocks of the continental interior, and in the region where the lithospheric thickness decreases on the eastern margin of the southern African cratons [Craig *et al.*, 2011].

[4] This paper will initially describe a source model for the 2006 Mozambique earthquake, derived from a joint inversion of seismic and geodetic data. The geodetically observed postseismic deformation is then considered in light of the distribution of coseismic slip. The longer-term deformation recorded by the tectonic geomorphology of the region is then described, followed by a discussion of the constraints our results provide on the rheology of the lithosphere in the region.

2. Coseismic Deformation

2.1. Methods and Previous Work

[5] The Mozambique earthquake has previously been studied in the field [Fenton and Bommer, 2006], by modeling teleseismically recorded P and SH waveforms [Yang and

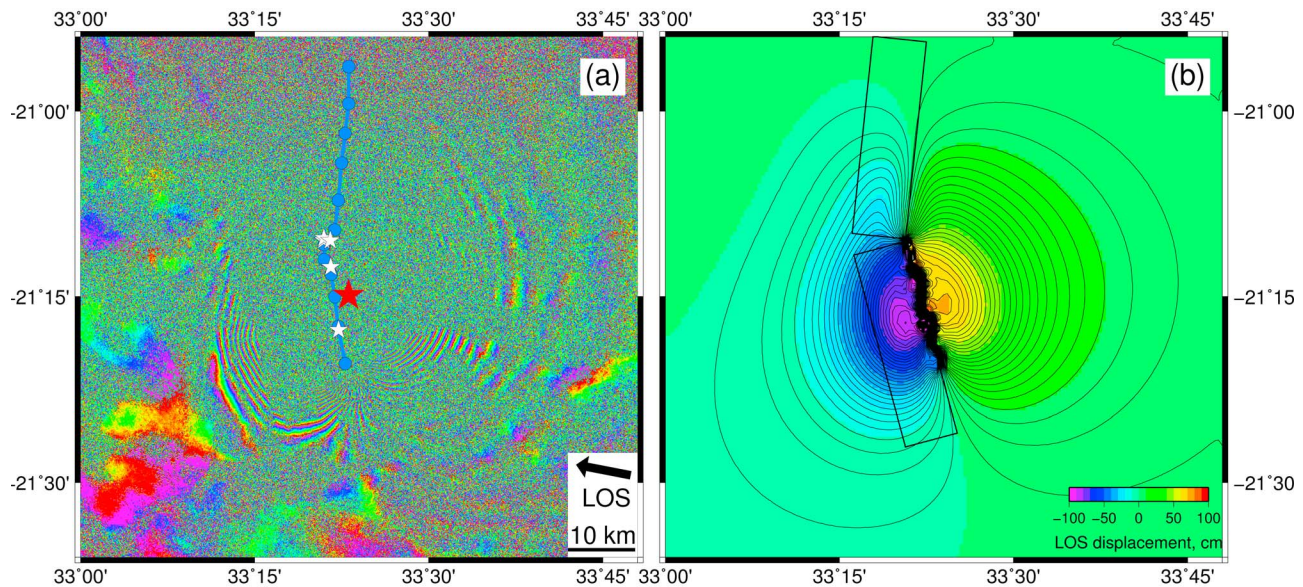


Figure 2. (a) Coseismic interferogram using descending-track Envisat data from 6th June 2004 and 7th May 2006. Each fringe represents 2.8 cm of line-of-sight (LOS) ground motion. As in Figure 1, the blue circles show the fault trace visible in the postseismic InSAR data (section 3), and the white stars show the locations of *Fenton and Bommer's* [2006] observations of surface faulting. The line of sight direction of the satellite is shown by the black arrow. (b) Synthetic line-of-sight displacements from the co-seismic slip model shown in Figure 3 (negative displacements correspond to increasing distance between the ground and the satellite). Each thin black line represents a synthetic InSAR fringe. The surface projections of the model fault planes are also shown.

Chen, 2008], and by using InSAR [*Fialko, 2009; Raucoules et al., 2010*]. This paper builds upon these previous studies by using all three data sources simultaneously, to perform a joint inversion for the source characteristics of the earthquake. By doing this we can minimize the trade-offs and, in some cases, poorly resolved source parameters that can result from using one data set alone. We can therefore produce a well-constrained model for the distribution of slip on the fault plane, which is one of the pieces of information that will allow us to investigate the rheology of the lithosphere in the region.

[6] We were able to create SAR interferograms for the time period spanning the earthquake using data acquired by the Envisat satellite (using the Caltech/JPL ROI-PAC software [*Rosen et al., 2004*]). The most coherent interferograms were formed by the images acquired on 9th November 2003 and 11th June 2006, and those from 6th June 2004 and 7th May 2006 (the earthquake occurred on 22nd February 2006). The interferogram for 6th June 2004 to 7th May 2006 is shown in Figure 2a, and is similar to the one formed by the other image pair. We were not able to unwrap the fringes in the region of high displacement gradients south of the fault in either of the interferograms, because the fringes were too closely spaced. We therefore split the InSAR data into four patches when performing our earthquake source inversions (i.e. separate eastern and western patches, from each of two interferograms). To account for the unknown offsets between the InSAR patches, as part of our inversions we solve for the relative displacement of each of the patches relative to an arbitrary reference value.

[7] We discretize the fault into $5 \text{ km} \times 5 \text{ km}$ cells and invert for the distribution of slip, rake, rupture velocity, and

risetime that best fit the InSAR displacements and the wavelet transforms of the seismograms, assuming a conceptual model in which the rupture nucleates at the hypocenter and propagates as a pulse with a finite width. We use a simulated annealing algorithm, and weight the seismic and geodetic data such that they have equal importance in the inversions, in the sense that the contribution of the weighted residuals of each type of data to the total misfit is equal. See *Ji et al. [2002]*, *Konca [2008]*, and *Konca et al. [2010]* for more detailed descriptions of the inversion technique. The surface intersections and strikes of the fault planes are constrained by the locations of surface slip seen in postseismic InSAR data (section 3), which are consistent with the mapped surface ruptures of *Fenton and Bommer [2006]* (and extend our knowledge of fault location into regions *Fenton and Bommer [2006]* were not able to visit). Based on the postseismic InSAR data, we use two fault planes with slightly different strikes, but both close to N-S (Figure 1). Throughout this manuscript these two fault planes will be referred to as the ‘northern’ and ‘southern’ fault planes, as indicated on Figure 1. In our inversions we impose that the slip in the shallowest cells must match the surface offsets measured by *Fenton and Bommer [2006]* in the locations where this data is available. In order to constrain the dip of the fault planes we have performed inversions to find the dip that best fits the seismic and geodetic data. For simplicity we assume the dip is the same for both planes. By performing inversions at 5° intervals we find the best fitting dip is 75° to the west, in agreement with the 76° proposed by *Yang and Chen [2008]* using teleseismic body-wave inversions.

[8] In order to locate the main shock hypocenter for use in our inversions, we have relocated the teleseismically

recorded aftershocks, and the main shock hypocenter, relative to each other using a multiple event relocation method that has been specialized for studies of calibrated (i.e. bias-free) locations. The earthquakes were first relocated in single event fashion using the EHB methodology [Engdahl *et al.*, 1998] with special attention to the analysis of depth phases to set focal depths for relocation (E. R. Engdahl, personal communication, 2010). We then used a method based on the Hypocentroidal Decomposition (HDC) method [Jordan and Sverdrup, 1981] to relatively relocate the events (see Biggs *et al.* [2006]; Bondar *et al.* [2008]; Nissen *et al.* [2010] for recent applications of this technique). The HDC analysis provides strong constraints on the relative locations of all events in the cluster (uncertainties are 1.1 to 7.2 km at the 90% confidence level, 34 of 41 events are less than 4.0 km). The resulting event distribution was then shifted so that the M_w 5.2 aftershock that occurred on 29th November 2007 lines up with the signal it produced in postseismic InSAR data (section 3). We assigned a circular region of uncertainty to this calibration location, with radius 3 km. By combining the uncertainties of the calibration location and the HDC-derived relative location of the events, we estimate that of the 41 events, 32 have final absolute location uncertainties of 5.0 km or less (longest semi-axis of the 90% confidence ellipse).

[9] The relocations show that the main shock hypocenter was in the southernmost fault plane (red star on Figure 1). We have varied the along-strike and down-dip location of the hypocenter within this region of the fault in order to find the best fit to the data. We find the best fitting depth was in an inversion cell extending from 15–20 km depth. This is in agreement with the reported ISC depth of 16.4 km, although deeper than the 11 km reported in the EHB catalogue. However, inversions in which the hypocenter is placed in the cell extending from 10–15 km depth show no significant differences from those shown below.

[10] The lack of geodetic data close to the fault means we are not able to accurately constrain the moment of the event. We therefore chose to use the value from the CMT solution of 4.5×10^{19} Nm. This is consistent with the USGS estimate of 4.6×10^{19} Nm, although larger than Yang and Chen's [2008] estimate of 3.5×10^{19} Nm. However, we view the moment estimates of the CMT and USGS to be more reliable because they used longer-period data than did Yang and Chen [2008], whose solution was based only upon body waves (which are less accurate for estimating the magnitudes of large events).

[11] There is a well-known trade-off between the smoothness imposed upon an inversion solution and the quality of fit to the data. As our preferred solution we select the smoothest model which involves only a minimal increase in the misfit to the data, choosing a similar point on the trade-off curve to numerous previous studies [e.g., Freymueller *et al.*, 1994; Johanson and Burgmann, 2010]. We will describe below the effects of imposing other values of the model smoothness.

2.2. Inversion Results

[12] Our inversion solution is shown in Figure 3. Fault slip was concentrated on the southernmost fault plane, reaching a peak of ~ 4.5 m at depths of 10–15 km. Significant slip

extended to depths of ~ 20 km, which is similar to the depths of the deepest aftershocks (Figure 1). The InSAR data is fit with an RMS misfit of 1.77 cm, which we view to be adequate because this is of a similar magnitude to commonly observed atmospheric effects. A comparison between the InSAR data and the model predictions is shown in Figure 3, and the line-of-sight displacements predicted by our slip model are shown in Figure 2b. We have also achieved a good match between the observed and modeled teleseismic P and SH waveforms, as shown in Figure 4 along with the source time function of the event. We find the rupture velocity to be in the range 2.2–2.4 km/s, similar to other large dip-slip earthquakes [e.g., Ji *et al.*, 2003; Avouac *et al.*, 2006; Copley *et al.*, 2011]. The centroid depth of our slip model is 13 km, which is close to the 12 km of the CMT solution and the 15 km of Yang and Chen [2008].

[13] The slip decreased from 10–15 km toward the surface. We view this feature of the inversions to be robust because if the slip at depth is limited to being the same as that observed at the surface by Fenton and Bommer [2006], the fits to the InSAR data are significantly worsened, even if the moment is allowed to change to the lower value found by Yang and Chen [2008] (an increase in misfit of 20% and 50%, for the CMT and Yang and Chen [2008] moment estimates). This is because the slip at depth is no longer sufficient to produce the observed displacement gradients. Because of the incoherent area close to the fault, the fit to the InSAR data is relatively unchanged if the amount of shallow slip is increased, and the teleseismic data is relatively insensitive to small changes in the magnitude of slip in this region. However, for the shallow slip to equal that required at depth to fit the more distant InSAR data, the surface slip would need to have been roughly twice the amount seen on the fault scarps measured by Fenton and Bommer [2006] (~ 3 – 4 m compared with the observed ~ 1 – 2 m). We think it unlikely that unobserved deformation away from the fault scarp would contribute the same amount of coseismic displacement as the slip on the observed fault (even in the presence of inelastic deformation in the material surrounding the fault [e.g., Kaneko and Fialko, 2011]), and are not aware of similar phenomena from other events. We therefore view the decrease in slip between depths of ~ 10 km and the surface as robust, and refer to this feature throughout the remainder of this paper as the 'shallow slip deficit'.

[14] In our model slip does not extend as far north as suggested by Raucoules *et al.* [2010]. This discrepancy is because we used teleseismic waveforms in addition to the InSAR data analyzed by Raucoules *et al.* [2010]. The distribution of coherent InSAR patches means that the slip in the northern part of the fault plane is not well resolved using the geodetic data alone. However, the teleseismic data does allow us to place constraints on the amount and distribution of slip that occurred on this northern plane, which must be minor compared with that on the southern plane. This issue will be discussed in greater detail below.

[15] The slip distribution shown in Figure 3 shows a ~ 15 km wide slip maximum, of relatively slowly varying displacement, with steep slip gradients on the margins: the same form as the analytic solution for slip on a circular crack. We therefore fit a profile through the slip distribution

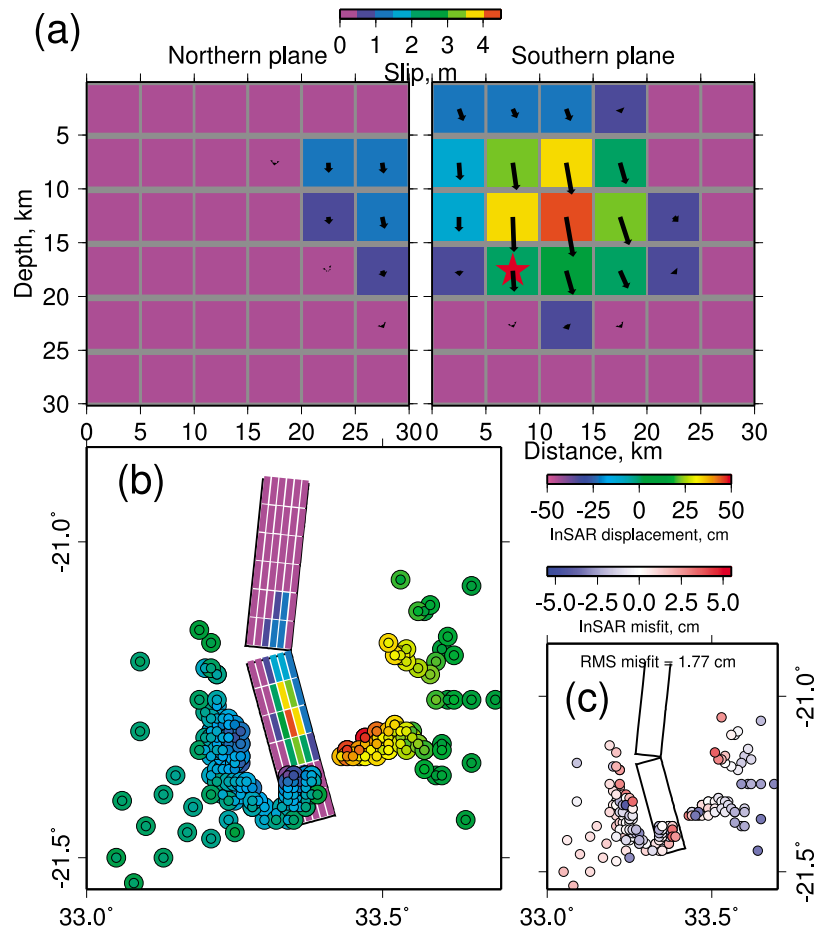


Figure 3. (a) The slip distribution in the 2006 Mozambique earthquake. The red star shows the hypocenter, and the colors represent the amount of slip. The arrows show the direction of motion of the hanging wall relative to the footwall. Depth is measured vertically from the surface. (b) Observed (large circles) and modeled (small circles contained within the observations) Envisat InSAR line-of-sight displacements (negative displacements correspond to increasing distance between the ground and the satellite). The slight variations in displacement on short length-scales (i.e. slight and non-systematic differences in color between adjacent points) are due to the InSAR data being from four different patches (section 2), each subject to different atmospheric effects and offsets relative to zero ground displacement. These offsets are solved for as part of the inversions. (c) The InSAR data minus the modeled displacements.

at a depth of 10–15 km with the expressions for constant stress-drop slip on a circular crack in a homogeneous elastic medium [e.g., *Eshelby, 1957; Burgmann et al., 1994*], in order to estimate the stress-drop in the earthquake (which controls the amount of slip for a rupture of a given size); this estimate is 16 MPa.

[16] In the auxiliary material we have included the results of inversions with different amounts of smoothness imposed upon the solution, and a graph of the trade-off between data misfit and model smoothness.¹ All of the models with an imposed smoothness that corresponds to an inversion result with a physically likely slip distribution (i.e. with no large variations of slip or rake occurring on very short length-

scales, beyond what would be expected for reasonable levels of fault stress heterogeneity), and which have misfits to the data that are not prohibitively large, share a number of common features. First, the slip is concentrated on the southern fault plane, with a slip maximum at depths of 10–15 km, and less slip in shallower and deeper cells. Additionally, the base of the rupture is at depths of 20–25 km.

3. Postseismic Deformation

3.1. Observations of Postseismic Deformation

3.1.1. Aftershocks

[17] Figure 5a shows the numbers and cumulative moments of the aftershocks that occurred following the main shock. The rate of events and the moment released was greatest immediately following the main shock. The activity then rapidly decreased until 250–300 days after the main

¹Auxiliary materials are available in the HTML. doi:10.1029/2011JB008580.

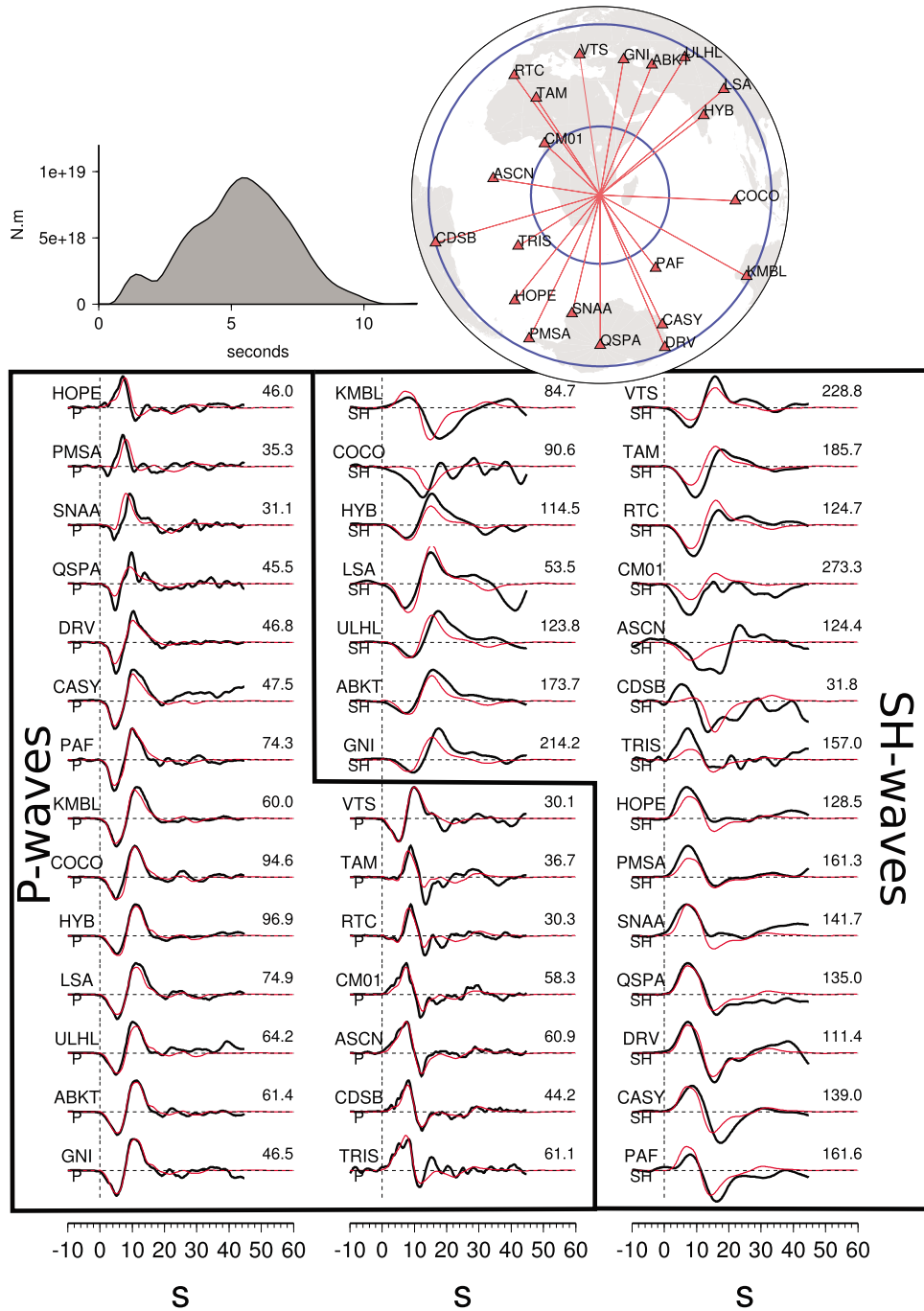


Figure 4. Observed (black) and modeled (red) teleseismic waveforms. Each trace is labeled with the station name, the type of wave (i.e. P or SH), and the maximum amplitude of the signal. The station distribution is shown in the upper right with the blue circles indicating epicentral distances of 30° and 80° . Also shown is the source time function of the event.

shock, followed by a more gradual lessening of moment release until the present-day. The total moment release by aftershocks to date is 3.7×10^{18} Nm, equivalent to a single M_w 6.3 event and 8% of the main shock moment. Figure 1b shows that the main concentration of aftershocks was toward the northern end of the southern fault plane, in the same region as the high slip patch in our coseismic source inversions.

3.1.2. Envisat Data

[18] We used Envisat and ALOS SAR data to construct interferograms for dates up until October 2010. Unfortunately, due to the large amounts of vegetation in the region, the Envisat data was not coherent enough to allow a continuous time series to be constructed. The only Envisat post-seismic interferogram with coherence over the fault covers a 35-day time window from 7th May to 11th June 2006 (74 to 109 days after the earthquake). This interferogram is shown

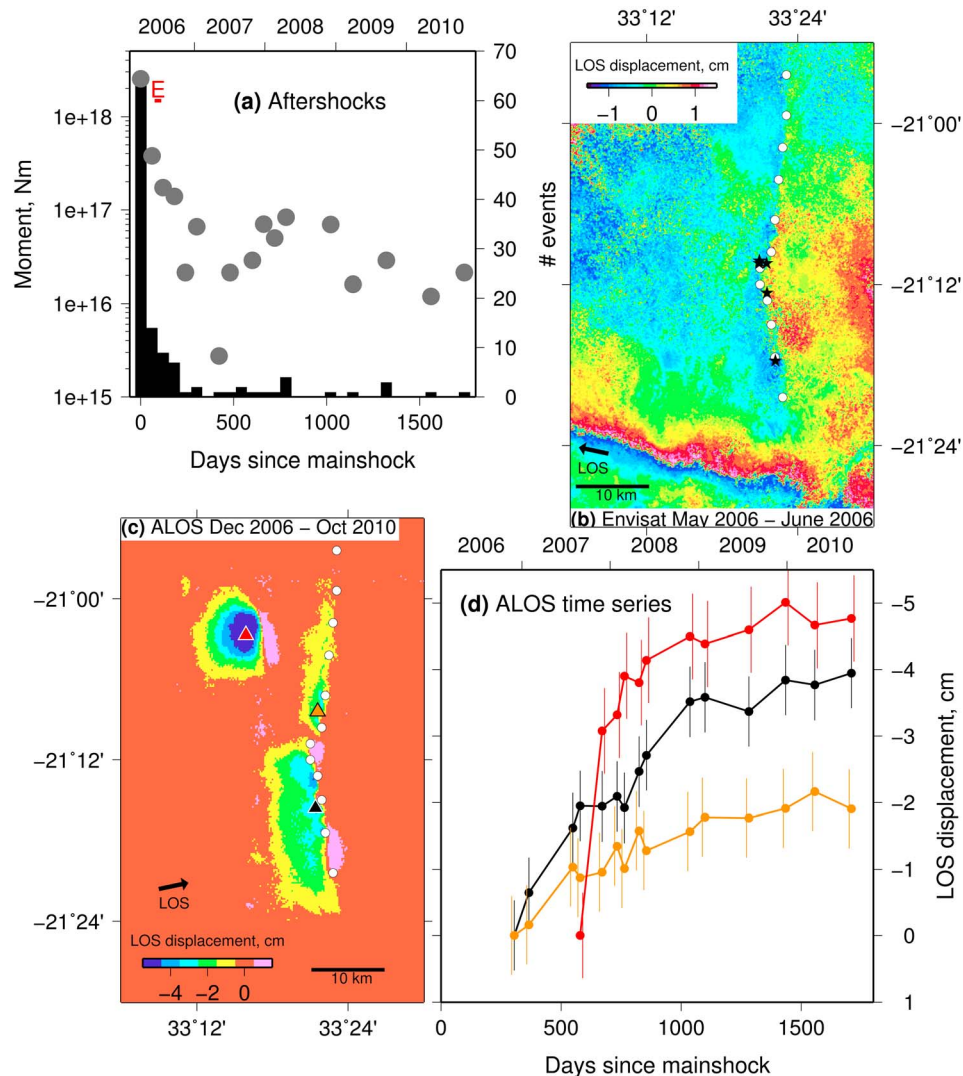


Figure 5. (a) The number of aftershocks (black bars) and the summed moments (grey circles) as a function of time after the main shock, summed over 60-day intervals. The red bar marked E shows the time span of the Envisat postseismic interferogram shown in Figure 5b. (b) Line-of-sight (LOS) postseismic displacements from an Envisat interferogram (negative displacements correspond to increasing distance between the ground and the satellite). The white circles show the location of a clear displacement discontinuity, and the black stars show the locations of surface faulting described by *Fenton and Bommer* [2006]. The E-W trending feature in the southern part of the image is an atmospheric effect. (c) Cumulative LOS displacements, relative to December 2006, measured by InSAR using ALOS data. This data has had atmospheric effects removed using the method described in the text. (d) The evolution of displacement through time for the three locations marked by colored triangles in Figure 5c.

in Figure 5b, and clearly shows a slip discontinuity which trends \sim N-S and matches the locations of surface faulting described by *Fenton and Bommer* [2006]. When discussing longer-wavelength postseismic deformation it is difficult to distinguish between viscoelastic flow beneath an elastic lid and continued slip on a discrete plane at depth [e.g., *Savage and Prescott*, 1978; *Freed and Burgmann*, 2004; *Perfettini and Avouac*, 2007]. However, the signal seen in Figure 5b represents a discrete step in the surface displacement field, and as such is only consistent with continued slip ('afterslip') on the shallow part of the fault plane, where it intersects the surface. The sense of slip is the same as that in the main shock.

3.1.3. ALOS Data

[19] The ALOS satellite gathered SAR data using a longer wavelength than the Envisat satellite, so the data is more coherent in vegetated areas such as the Mozambique coastal plain. We were therefore able to create interferograms from the date of the first ALOS acquisition in the region (December 2006) up until October 2010, all of which are coherent in the region of the fault. We constructed 60 interferograms from 15 SAR scenes. We then used a least squares algorithm to solve for the temporal evolution of displacement, relative to the first scene, at each pixel and at each SAR acquisition date. The signal due to postseismic deformation is up to ~ 4 cm in magnitude, which is roughly

double the observed atmospheric effects. From visual inspection of the interferograms, and from stacking the data, it appears that no temporally consistent signals are present except for in the regions of the fault planes and one shallow aftershock, suggesting no resolvable tectonic deformation occurs away from these areas. We have attempted to remove the apparent displacements due to atmospheric signals. To do this we fitted a smoothly varying displacement field to the signal at each SAR acquisition date, not including the regions of tectonic deformation. We then extrapolated this ‘atmospheric’ displacement field across the previously excluded regions of tectonic deformation using splines in tension [Smith and Wessel, 1990], and then removed the extrapolated atmospheric signal from the whole image to leave just the tectonic signal remaining. The total deformation observed over the date range December 2006 – October 2010 is shown in Figure 5c, and the evolution through time of the deformation at three points is shown in Figure 5d. These time series of data show that some atmospheric effects still remain (the short-term fluctuations), but the overall signals are of the temporally smooth form expected for tectonic deformation. The method we have used to remove the atmospheric signals is relatively crude. However, the similar magnitudes of the atmospheric and tectonic signals, and the lack of ‘ground-truthing’ GPS data, meant that we were not successful in isolating the tectonic signal using more sophisticated methods [Kositsky and Avouac, 2010]. Additionally, we did not want to follow the commonly used approach of assuming a functional form of the tectonic displacement in order to extract this signal, because we did not want to impose constraints upon the estimated time-evolution of the deformation. The apparent displacements before the removal of atmospheric effects, along with an equivalent to Figure 5d produced from the uncorrected measurements, are shown in the auxiliary material.

[20] Figures 5c and 5d show that there are three locations of significant postseismic deformation. The first is adjacent to the southernmost fault plane, where the coseismic slip was concentrated (Figure 3). The evolution of deformation shown in black on Figure 5d demonstrates that the rate of displacement accumulation in this location was approximately constant at ~ 17.5 mm/yr throughout 2007 and 2008 (in agreement with the findings of *Raucoules et al.* [2010]). This rate is considerably faster than the long-term extension rate of ~ 2.5 mm/yr across the entire plate boundary [Nocquet et al., 2006], of which this fault forms only a part. Shortly after 1000 days post main shock (late 2008) the deformation became unresolvably slow or stopped. The region of resolvable postseismic surface deformation does not extend far enough from the fault to coincide with the areas where the coseismic Envisat interferograms were coherent. We are therefore confident that any postseismic deformation present in the coseismic interferograms will be minor compared with the large coseismic displacements, and that the slip inversions are not likely to be significantly contaminated with postseismic signals.

[21] The second region of displacement accumulation was near the northern fault plane. The evolution of postseismic displacement shown in orange on Figure 5d displays a similar behavior to that seen adjacent to the southern part of the fault plane, with a relatively rapid rate of displacement

accumulation followed by slow motion or the cessation of deformation. This deformation will be discussed in greater detail below (section 3.2) in light of the deformation measured in the region using optical satellite images.

[22] The third observed postseismic deformation signal is that caused by a shallow $M_w 5.2$ aftershock that occurred on 29th November 2007. The evolution of displacement in this region is shown in red on Figure 5d. The sudden displacement in the aftershock was followed by ~ 275 –450 days of motion at progressively decreasing rates. This timescale is similar to that over which aftershock activity died away after the main shock, suggesting a common postseismic deformation mechanism. It was the InSAR signal of this aftershock that was used to geographically locate the relatively relocated aftershocks and main shock hypocenter (section 2).

3.1.4. SPOT Optical Data

[23] We have also measured surface deformation in the region of the earthquake by cross-correlating SPOT 5 optical images using the Cosi-Corr programme of *Leprince et al.* [2007, 2008]. The two images we used were acquired on 3rd August 2001 and 26th August 2008, so the measured deformation spans the coseismic and postseismic time periods (ending close to the date that the ALOS InSAR data shows the surface deformation rate decreased or stopped). The method we have used usually measures the deformation in two perpendicular directions, East-West and North-South. However, in this case the incidence angle of the satellite images we used was not vertical, which means that vertical ground motions show up as an apparent displacement in the E-W component. Specifically, because the satellite was looking to the west, uplift will appear as a negative eastward signal with a magnitude given by the vertical displacement multiplied by the tangent of the incidence angle (see *Copley et al.* [2011] for a more complete discussion of the interpretation of optical image correlation data with non-vertical incidence angles). For the images we used the incidence angle is $\sim 20^\circ$, resulting in the vertical motions being multiplied by ~ 0.36 . In the measurements produced using the Cosi-Corr method, the absolute values of the displacement are not well constrained, but the magnitudes of displacement discontinuities are robust features.

[24] In the region of the southern fault plane, where the coseismic slip was concentrated, there is little evidence for N-S displacements, which is as would be expected given the minimal N-S displacements in our coseismic slip models and observed in the field. There is also no clear discontinuity in the E-W displacements, which is also as expected because for steeply dipping dip-slip faults the fault-perpendicular displacement discontinuity at the surface is small. Additionally, for the image geometry we used the E-W displacements result in a signal of opposite sign to the vertical motions, so the two signals destructively interfere. The coseismic slip model shown in Figure 3 would result in a signal in the E-W component of ~ 25 cm, which is below the detection threshold of ~ 50 cm for 5 m resolution SPOT5 images.

[25] Figures 6a and 6b show that ~ 1 m of left-lateral strike-slip motion accumulated on the northern fault plane during the time span of the images, and that there is no resolvable E-W displacement discontinuity. We have investigated if this slip could be coseismic by imposing the observed deformation on the northern fault plane during

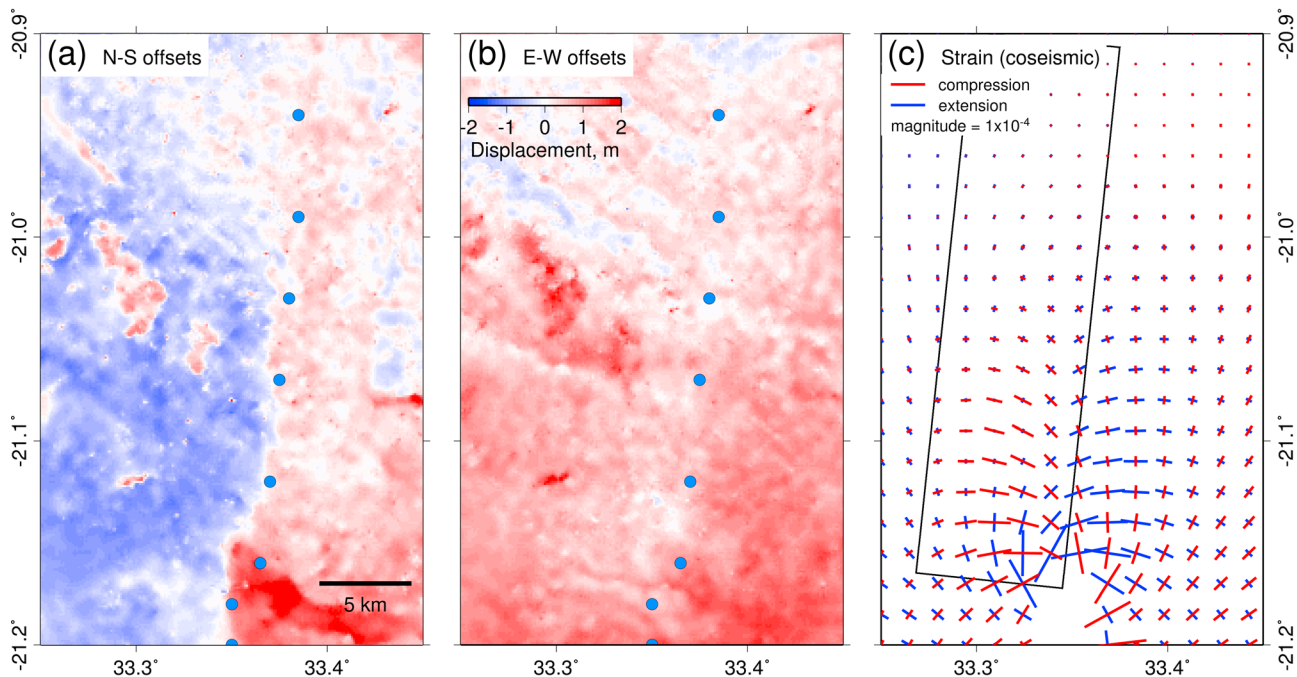


Figure 6. (a, b) N-S and E-W surface displacements measured from the cross-correlation of SPOT satellite images. Northward and eastward motions are positive. The robust outputs of this method are displacement discontinuities, not the absolute displacement values or long-wavelength features. As such, the robust feature is the roughly N-S trending discontinuity seen in the N-S offsets, equivalent to left-lateral strike-slip. The blue circles show the location of the displacement discontinuity observed in the postseismic Envisat interferogram (Figure 5). (c) Principal axes of the horizontal strain tensor at the surface, calculated from the coseismic slip model (Figure 3). Also shown (black lines) is the surface projection of the (west-dipping) northernmost fault plane.

some coseismic source inversions. We have constrained the strike-slip component of motion to be 1 m, and varied the dip-slip component (which the optical image results are much less sensitive to) so that the rake varies between pure left-lateral strike-slip and -60° . If slip is imposed on the northern plane from the surface down to a depth of 15 km, then the misfits between the observed and modeled teleseismic waveforms become significantly higher than in our preferred model (by 11–35%, as the rake varies from left-lateral strike-slip to -60°). These misfits take the form of systematic differences in shape and magnitude between the observed and synthetic waveforms, and are due to significant moment being released at times later than is consistent with the source time function of the event. For slip extending to a depth of 10 km, the corresponding values are 7–18%. Lower amounts of coseismic slip on the northern plane result in lower misfits between the model and the teleseismic and InSAR data (until the best fitting model is reached, where only minor slip, and normal in sense, occurs on the northern plane; Figure 3). The degree to which any coseismic slip could have occurred on the northern plane depends upon the resolution of the teleseismic waveforms to small amounts of slip in this region. Our inversions suggest that we can exclude significant moment release (e.g. the surface deformation observed in the SPOT data, extending down to 10 km or more), but not the possibility that some minor slip may have occurred in a small number of the inversion cells (e.g. 1–2 m in up to ~ 5 cells). We therefore cannot conclusively say to what extent the slip observed in the SPOT

data accumulated coseismically (the increases in misfit to the teleseismic data for slip in only the top 5 km of the northern fault plane are insignificant, i.e. 0.7–2.3%). However, we think it unlikely that the rupture propagated horizontally for the ~ 20 km observed in the SPOT data, within only the top 5 km of the fault plane, given that this is the depth range that partially arrested the rupture on the southern fault plane. We do know that at least some of the deformation is definitely postseismic afterslip, as demonstrated by the signal seen in the postseismic Envisat and ALOS data in this region. However, it is possible that some of the slip adjacent to the southern fault plane could be coseismic.

3.2. Interpretation of Postseismic Deformation

3.2.1. Southern Fault Plane

[26] By inverting the displacement field adjacent to the southernmost fault shown in Figure 5c, it is possible to estimate the slip on this fault plane over the time period covered by the postseismic ALOS InSAR data. In these inversions we use cells with lengths and widths of half that used in the main shock inversions (i.e. 2.5 km), in order to allow us to use the near-source InSAR data to constrain the details of the shallow slip. The results of this slip inversion show ~ 10 cm of normal-faulting motion on the upper ~ 10 km of the fault plane (Figure 7), equivalent to a moment magnitude of 5.7. The depth extent of the afterslip corresponds to where the coseismic slip decreased from depths of ~ 10 km toward the surface (Figure 3), suggesting

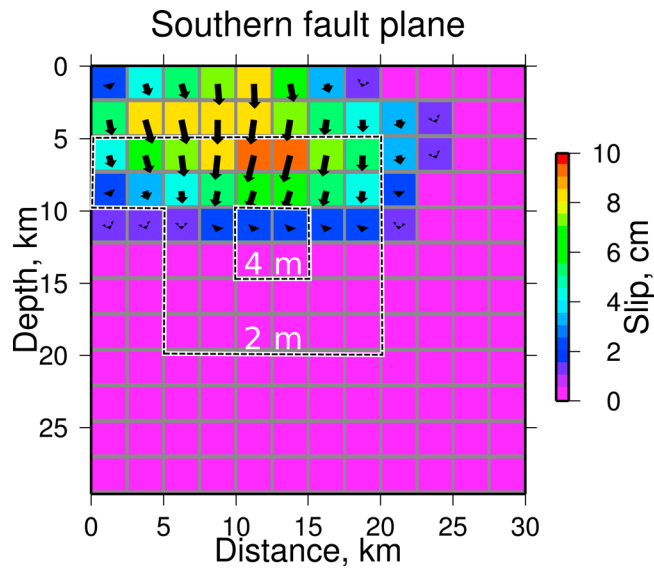


Figure 7. Distribution of postseismic afterslip on the southern fault plane during the time period covered by the ALOS SAR data (~ 300 – 1700 days post main shock). The location and size of the fault plane is the same as that shown in Figure 3, but the individual cells are half the width and height. The 4 m and 2 m contours from the coseismic slip model are also shown.

that the afterslip is ‘filling in’ the coseismic shallow slip deficit. However, the slip we have inferred from the ALOS data (~ 10 cm) is much smaller than the shallow slip deficit (~ 1 – 2 m). In order to estimate what proportion of the slip deficit has been recovered we need to estimate the amount of shallow afterslip that occurred between the main shock in February 2006 and the start of ALOS data acquisition in December 2006. One method of making this estimate is to make assumptions regarding the functional form of the surface deformation [e.g., *Fialko, 2004; Chandrasekhar et al., 2009*]. The Envisat data shows that the average rate of deformation between 74 and 109 days after the main shock (0.6 mm/day) was considerably faster than the roughly linear rate of 0.05 mm/day seen in the ALOS data. This rapid rate seen in the Envisat data coincides with the time of frequent aftershocks shortly following the main shock (Figure 5a). Geodetic data following large earthquakes shows that ground displacements often follow a logarithmic function [e.g., *Langbein et al., 1983; Hsu et al., 2006, 2009*]. We have therefore assumed that the surface displacements were logarithmic in form until 250 days after the main shock, when the aftershock activity had decayed to low rates (Figure 5a). We then found a logarithmic function that replicates the 2.2 cm displacement observed in the Envisat interferogram from May–June 2006. To the displacement calculated in this manner, we added a displacement calculated from the linear rate of deformation seen in the ALOS data, which we assumed to occur from 250 days after the main shock until the rate of displacement decreased in late 2008. Using this method we estimate that the total afterslip is roughly an order of magnitude greater than is observed in the time period covered by the ALOS data (i.e. on the order of meters). There are obviously large

uncertainties inherent in this estimate. Therefore, the only conclusion we would like to draw from this extrapolation is that the InSAR data is potentially consistent with the decrease in deformation rate in late 2008 corresponding to the time when the shallow afterslip had removed the shallow slip deficit observed in the coseismic slip model. However, this is by no means necessarily the case, and afterslip is often observed to not completely recover the shallow slip deficit [e.g., *Fialko, 2004; Fielding et al., 2009*].

3.2.2. Northern Fault Plane

[27] The strike of the northernmost fault plane, which is perpendicular to the regional extension direction, and sub-parallel to the southern fault plane, suggests that the motion on the fault is usually dominantly dip-slip rather than strike-slip. The tectonic geomorphology in the region also indicates dip-slip faulting on this plane (section 4). However, a potential explanation for the significant left-lateral strike-slip component of motion observed in the SPOT image correlations (Figure 6a) lies with the stresses induced by slip on the southern fault plane. Figure 6c shows the principal axes of the horizontal strain tensor at the surface, calculated from the elastic displacements predicted by the coseismic slip model. The coseismic strains in the region of the northern fault plane are equivalent to left-lateral strike-slip on N-S planes. The agreement between this calculated sense of strain and the slip observed by the SPOT image correlation suggests that the northernmost fault plane accumulated displacement in response to the stresses generated by the slip on the southernmost fault plane (although we cannot conclude if all of this signal was postseismic, or if some of the deformation resulted from the propagation of coseismic slip into the region). This view is supported by the observation that the coseismic strains and the deformation measured using the SPOT images both decay over a similar distance of 15–20 km along the northernmost fault. For the displacements produced by the slip on the southern fault plane to produce offsets of ~ 1 m across the northern fault plane, the recovery of the shallow slip deficit would be required to be almost complete, which is at odds with observations from other events [e.g., *Fialko, 2004; Fielding et al., 2009*]. This may suggest that some coseismic slip did propagate into the northern fault plane (as discussed above), which would then provide additional driving stresses for the afterslip in the region.

[28] We can draw further conclusions based on comparing the InSAR and SPOT data for the region of the northernmost fault plane. The ALOS InSAR data indicates an increase in range between the satellite and the ground on the western side of the fault, which is the opposite expected for pure left-lateral strike-slip on a N-S plane. This discrepancy suggests that some normal-sense slip occurred, as is also suggested by the mechanisms of the two aftershocks that occurred close to the northern fault plane (Figure 1). The viewing geometry of the ALOS satellite constrains this normal component to be more than 17% of the strike-slip motion during the ALOS observation period. Given that normal motion on a steeply dipping fault will produce a small E-W signal, which is largely canceled out by the signal resulting from the vertical motions (as described above), this small percentage is well beneath the detection threshold on the E-W component of the SPOT image correlation. Unlike the optical image

correlation data, the InSAR data is sensitive to the length-scale over which the deformation decays away from the fault trace. This length-scale is similar to the InSAR signal near the southernmost fault plane (the signal is roughly half the amplitude, and decays to unresolvable levels in roughly half the horizontal distance; Figures 5c and 5d). It is therefore likely that the afterslip observed in the ALOS data occurred over a similar depth range to that on the southernmost fault plane, from the surface to depths of ~ 10 km.

3.2.3. Aftershock

[29] The red line on Figure 5d shows a roughly logarithmic decay of displacement following the aftershock visible in the ALOS SAR data. The timescale of this deformation is similar to the period of high aftershock activity and rapid motion on the southern fault plane following the main shock, suggesting a common deformation mechanism. We assume that the deformation following the aftershock represents afterslip, which seems likely given the shallow depth (well above the 20 km depth of the deepest aftershocks, and so the likely brittle-ductile transition depth). We can investigate the material properties of the fault by using the expressions of *Perfettini and Avouac* [2004], which are based upon rate-and-state friction considerations. We have fit to the ALOS displacements the equation $U(t) = U_c + \beta V_0 t_r \log[1 + d(\exp(t/t_r) - 1)]$ where $d = \exp[\Delta CFF/(a\sigma)]$ and $U(t)$ is the measured displacement through time, U_c is the coseismic offset in the aftershock, β is a geometrical factor, V_0 is the interseismic slip rate, t_r is the relaxation time, ΔCFF is the coulomb stress change due to the aftershock, and σ is the average normal stress on the fault plane. a is a frictional parameter that represents the dependence of the coefficient of friction on the rate of deformation, i.e. $\mu = \mu_* + a \ln(V/V_*) + b \ln(\theta V_*/d_c)$ where μ is the coefficient of friction, V is the sliding velocity, θ is a fault state variable, d_c is a constitutive parameter, and subscript stars represent values defined at an arbitrary sliding velocity. Following *Perfettini and Avouac* [2004] we have assumed that $b = 0$ and so neglected the ‘state’ dependence of friction. If a is positive [e.g., *Dieterich and Kilgore*, 1994], this assumption imposes that $(a - b)$ is positive, which leads to a ‘rate-strengthening’ rheology in which a fault will undergo steady sliding in response to applied forces (in keeping with the postseismic deformation mechanism being afterslip). In the region where the aftershock nucleated, which is likely to be offset from the location of afterslip (as was the case for the main shock), the frictional properties must have been different so that $(a - b)$ could be negative and the fault could act in a stick-slip manner. We find that because of our lack of information regarding the coseismic offset in the aftershock, and the scatter in the data, all of the unknown model parameters can be varied within wide ranges and still fit the data to a given tolerance. We are therefore only able to infer that d lies in the range $1 \times 10^5 - 3 \times 10^6$, which means that the value of a is $1 \times 10^{-3} - 2 \times 10^{-2}$ (assuming the coseismic stress change was in the range 1–10 MPa, and that the normal stress is lithostatic at 2 km depth, either with or without hydrostatic pore fluid pressures). This estimate is comparable to the values of $5 \times 10^{-3} - 1.5 \times 10^{-2}$ suggested by laboratory experiments [e.g., *Dieterich and Kilgore*, 1994], and (assuming that $b = 0$) with the estimates of $(a - b)$ of $1 \times 10^{-3} - 3 \times 10^{-3}$ made by *Hearn et al.* [2002] following the Izmit

earthquake, $1.3 \times 10^{-3} - 1 \times 10^{-2}$ made by *Perfettini and Avouac* [2004] following the Chi-Chi earthquake, and $10^{-4} - 10^{-3}$ made by *Johnson et al.* [2006] using the post-seismic deformation of the Parkfield earthquake.

3.3. Summary of Postseismic Deformation

[30] In summary, postseismic deformation was observed to occur at two different rates following the Mozambique earthquake. The numbers of aftershocks and the rate of motion observed in the Envisat interferogram show that rapid deformation occurred shortly after the main shock, for ~ 250 days. There was then a prolonged period of deformation at an approximately constant rate, which ended in late 2008, roughly 1000 days after the earthquake. This deformation took the form of afterslip in the upper ~ 10 km of the coseismic fault plane. On the northern fault plane, postseismic afterslip took place over a similar depth range, but in this case the motion had a significant strike-slip component, and appears to have been relaxing the stresses generated by the slip on the southernmost fault plane (and possibly also some coseismic slip on the northern fault plane). In this sense, although the rakes were different, the shallow parts of both fault planes can be seen to be acting in the same manner, by slipping in response to the stress changes produced by fault motion.

4. Tectonic Geomorphology

[31] This section considers the tectonic geomorphology in the region of the earthquake. *Fenton and Bommer* [2006] concluded, based on field observations, that geomorphological indicators of the presence of active faulting were too subtle to permit the fault to be identified without the information provided by the earthquake itself. However, the use of satellite images and elevation data allows subtle geomorphic features to be observed that are sometimes not clearly identifiable during fieldwork because of their spatial extent [e.g., *Goldsworthy et al.*, 2002; *Copley and Jackson*, 2006]. In addition, time constraints and mine fields limited the regions of the fault that *Fenton and Bommer* [2006] were able to visit, so an examination of remote sensing data allows a greater proportion of the fault to be studied. This section describes the geomorphology of the fault that ruptured in the Mozambique earthquake, indicating ways in which similar fault systems can be identified before they break in future earthquakes.

[32] Figure 8a shows the topography in the region of the northernmost fault plane. The regional topography slopes from west to east, and there is a clear reversal of slope visible at the fault which has deflected the course of the local drainage (Figures 8a and 8b). The reversal of slope is equivalent to a 15 m vertical offset of the ground surface, and is consistent with the inference that the northernmost fault plane usually accommodates normal-faulting motion (E-W extension). Figure 8c shows a satellite image of the junction between the northern and southern fault planes. An ephemeral lake is observed on the western (downthrown) side of the fault (marked ‘L’), suggesting that the river running through the region has been dammed by vertical motions on the fault. Additionally, on the southernmost fault plane, an ephemeral pond (marked ‘P’) and a small linear valley (marked ‘V’) are also seen on the downthrown side.

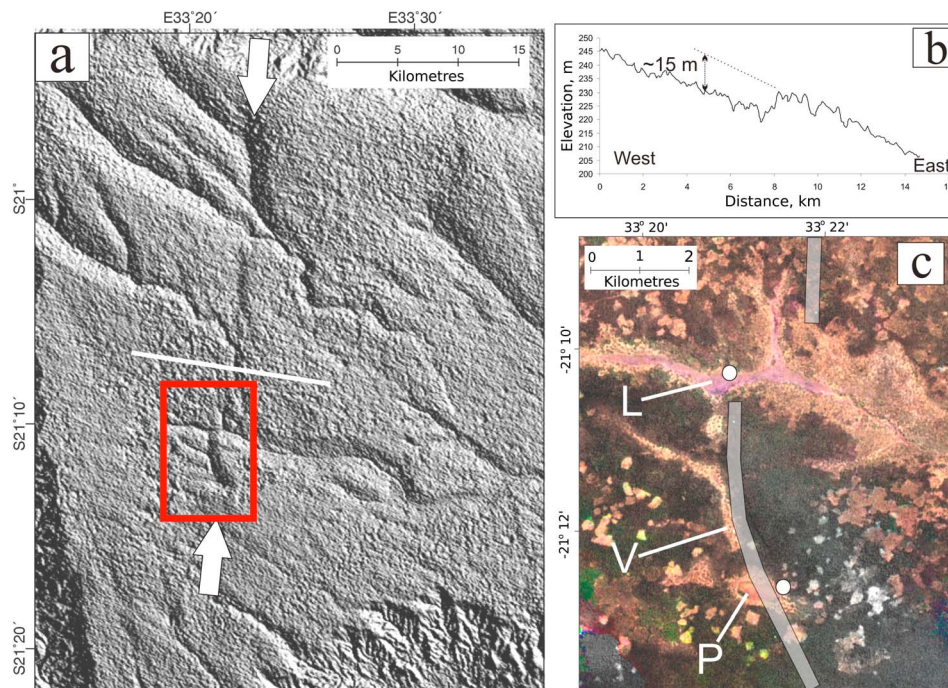


Figure 8. (a) Topography in the region of the Mozambique earthquake, illuminated from the east. The white arrows show the location of a \sim N-S trending scarp that reverses the regional downward slope to the east. This scarp corresponds to the location of the northern fault plane shown in Figure 1b. (b) Topographic profile along the white line in Figure 8a. The scarp is clearly visible, and represents a \sim 15 m vertical offset in the regional slope. (c) Landsat satellite image of the region marked by the red box in Figure 8a (Band combination: red = 3, green = 2, blue = 1, intensity from band 8). White circles show the locations of surface ruptures identified by *Fenton and Bommer* [2006]. Grey bands show the approximate locations of the surface displacement discontinuities in the Envisat postseismic interferogram shown in Figure 5b. Also labeled are an ephemeral lake and pond (L and P), and a shallow linear valley (V).

The combination of the reversal of slope and the damming of local drainage are indicative of the presence of previous faulting, and so provide a method of identifying other active faults within the region. Using these indicators, active faults to the NE of that which ruptured in the earthquake have been identified and marked with white arrows on Figure 1b.

5. Discussion

5.1. Upper-Crustal Rheology

[33] The coseismic and postseismic results indicate that on the southern fault plane the top \sim 10 km of the crust accumulated less slip during the earthquake than deeper depths, and then slipped postseismically. This shallow coseismic slip deficit implies the shallow part of the fault inhibited the propagation of seismic rupture, although some coseismic slip did occur. The depth range over which the coseismic slip deficit and the ensuing shallow afterslip occurred roughly corresponds to the 5–10 km thickness of sediments in the Mozambique coastal plain [*Salman and Abdula*, 1995; *Watts*, 2001]. It therefore appears that the fault plane has different mechanical properties where it cuts through the thick sequence of sediments, compared to deeper depths where it cuts through crystalline basement.

[34] The behavior we have observed is similar to that expected for a fault zone in which a ‘velocity-weakening’ region (which will display stick-slip behavior) is separated from the surface by a ‘velocity-strengthening’ region (which will usually slide at slow velocities in response to applied stresses, and not accumulate elastic strain) [e.g., *Marone et al.*, 1991; *Rice*, 1993; *Kaneko et al.*, 2008]. Numerical models [e.g., *Kaneko et al.*, 2008] show that in this situation coseismic rupture can dynamically propagate into the velocity-strengthening region, although the total slip will be lower than in the velocity-weakening region beneath. In such a situation the velocity-strengthening surface layer would then be expected to slide in the time following the earthquake, in response to the coseismic stress changes, as is observed for the case of the Mozambique earthquake. The significant strike-slip motion observed on the northernmost fault plane suggests that the stresses generated on that part of the fault during the earthquake were similar to, or larger than, the \sim E-W extensional stresses related to the motions of the bounding plates, probably indicating that the shallow part of the fault was relatively unstressed prior to the earthquake.

[35] If the link between our observations, the thickness of the sedimentary layer, and the dynamic models of afterslip are correct, then we can infer that the rock-type a given fault

is cutting plays a first-order role in determining whether it will display stick-slip (velocity-weakening) or predominantly creeping (velocity-strengthening) behavior. Shallow slip deficits have been observed in other earthquakes [e.g., *Fialko et al.*, 2005, and references therein], and it may be that similar effects occur in the sedimentary layer in most earthquakes (as also suggested by *Marone et al.* [1991]), but that the large thickness of sediments in the region of the Mozambique earthquake allowed the behavior to be seen with greater ease. With the information we have available we are not able to infer exactly what property of the fault or surrounding rocks and fluids in the sedimentary layer promotes creeping rather than stick-slip behavior. One possibility is suggested by the experiments of *Marone et al.* [1990], which demonstrated that unconsolidated gouge can behave in a velocity strengthening manner. However, it should also be noted that some experimental results show that fault gouge can become velocity weakening under certain conditions of displacement and induration [e.g., *Biegel et al.*, 1989], which may explain why earthquakes do sometimes nucleate in (and are contained within) the sedimentary layer [e.g. *Nissen et al.*, 2011].

5.2. Mid-crustal Rheology

[36] The coefficient of friction (the ratio of shear and normal stresses at failure) for rocks is generally thought to be in the range between 0.6 ('Byerlee's Law') and ≤ 0.1 [e.g., *Lamb*, 2006; *Herman et al.*, 2010; *Copley et al.*, 2011]. These coefficients of friction are expected to result in active normal faults forming at dips between 60° and 45° , which may then rotate to shallower dips during the accumulation of displacement. The dip of the fault that ruptured in the Mozambique earthquake ($\sim 75^\circ$) is therefore steeper than expected. This steep dip is likely to represent the rupture of a preexisting weak plane where slip can occur at lower stresses than on more optimally oriented, but stronger, planes. The extensive faulting in the region that occurred during the break-up of Gondwana may be the origin of this preexisting weakness.

[37] We can quantify the weakness of the fault plane relative to the surrounding material by comparing the coefficient of friction required for slip on a 75° plane with that on an optimally oriented plane in the same location (which may or may not be a preexisting fault). If the coefficient of friction of the optimally oriented planes were 0.6 (as in 'Byerlee's Law'), then these planes would dip at 60° , and the fault that broke in the earthquake would be required to have a coefficient of friction at least $\sim 25\%$ lower. If the coefficient of friction for the optimal planes were the lower value of 0.1 (as suggested by some geophysical observations [e.g. *Lamb*, 2006; *Herman et al.*, 2010; *Copley et al.*, 2011]), then the optimal planes would dip at 48° , and the fault that ruptured would be required to have a coefficient of friction at least $\sim 45\%$ lower. In these calculations we have assumed that the fault plane has a homogeneous coefficient of friction throughout. It has been suggested that faults may be 'statically strong but dynamically weak' [e.g., *Lapusta and Rice*, 2003; *Di Toro et al.*, 2004], i.e. containing weak patches in which slip can nucleate and spread by dynamic weakening into regions not at the static failure criterion. If this is the case, then our

constraints upon the coefficient of friction apply to the weak regions of the faults, where the slip first nucleates.

[38] The Mozambique earthquake ruptured from the surface to a similar depth as the 2001 $M_w 7.6$ Bhuj (India) earthquake [*Copley et al.*, 2011] ($\sim 25\text{--}30$ km at Bhuj and ~ 20 km at Mozambique), and the along-strike extent of the high-displacement patch was relatively similar in size (~ 25 km at Bhuj and ~ 20 km at Mozambique). Both are dip-slip events in relatively slowly deforming regions, although the Bhuj event was a thrust. The considerably lower displacements in Mozambique compared with Bhuj mean that the stress-drop we have estimated is roughly a factor of two lower than that seen at Bhuj (~ 35 MPa at Bhuj compared with ~ 16 MPa at Mozambique), which is likely to be a robust feature because both estimates were obtained using the same techniques so no methodological biases should be present. One possible explanation for the difference is that the estimated stress-drop represents an average over the ruptured patch, and if the shallow part of the fault plane in Mozambique obeys a different rheological law (i.e. velocity-strengthening rather than velocity-weakening), then the calculations of *Kaneko et al.* [2008] suggest a reduced stress-drop on the shallow part of the fault. (Although there was a shallow slip deficit apparent in co-seismic models of the Bhuj event, it occupied a smaller proportion of the vertical rupture extent.) Another possibility is that the two fault planes simply have different material properties, because of differences in mineralogy or pore fluid pressures. *Copley et al.* [2011] suggested that the Bhuj fault plane was strong enough to support the forces exerted upon India by the Tibetan Plateau (equivalent to the suggestions of *Townend and Zoback* [2000] and *Jackson et al.* [2008] that the majority of lithospheric stresses are transmitted through the seismogenic layer). This logic implies that if there are variations by up to a factor of two in the shear stresses supportable by faults in the seismogenic layer, then the processes responsible for these differences could play a role in halving or doubling the sizes of stresses that can be transmitted through the continents, and so the topography that can be supported. Therefore, if the mechanical properties of the sedimentary layer are playing a fundamental role in governing fault rheology at shallow depths, then the location and thickness of sedimentary deposition could have a dramatic effect upon large-scale continental tectonics (in a manner additional to the temperature effects that *Copley et al.* [2009] discussed in the Adriatic region).

5.3. Rheology of the Ductile Lithosphere

[39] As described above, there was no resolvable long-wavelength postseismic deformation signal of the type often observed after large earthquakes [e.g., *Freed and Burgmann*, 2004], as was also concluded by *Fialko* [2009] and *Raucoles et al.* [2010]. This lack of signal can be used to place constraints upon the viscosity of the ductile lithosphere in the region. We have used the VISCO-1D code [*Pollitz*, 1992] to calculate the postseismic response of a Maxwell viscoelastic layer underlying an elastic lid, in response to the stresses generated by our coseismic slip model. Based on the depth extent of the main shock, and the depth distribution of aftershocks, we use an elastic layer extending to a depth of 21 km (1 km deeper than the estimated base of the coseismic

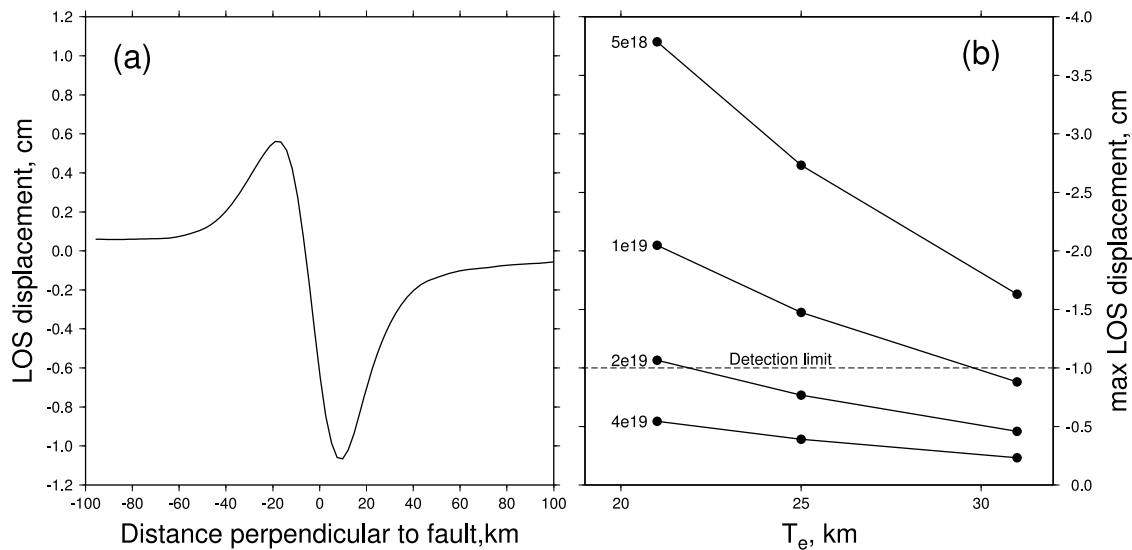


Figure 9. (a) Predicted ALOS line-of-sight displacement along a profile through the center of the fault over the time period December 2006 to October 2010, calculated assuming relaxation in a Maxwell viscoelastic half-space with a viscosity of 2×10^{19} Pa s underlying a 21 km thick elastic layer (negative displacements correspond to increasing distance between the ground and the satellite). (b) Maximum line-of-sight displacement as a function of the thickness of the elastic layer and the viscosity of the underlying half-space. Our detection limit of 1 cm is shown.

slip and the deepest aftershock, in order to avoid numerical problems resulting from the fault reaching the base of the elastic layer). We have used two conceptual models of lithosphere rheology in order to constrain the viscosity of the ductile layers. In the first we have assumed that the entire ductile lithosphere has the same viscosity, and have found the minimum viscosity that would result in no visible post-seismic deformation at the surface during our period of ALOS observations (December 2006 to October 2010). Based on the ALOS data presented above, we assume a detection limit of 1 cm. This limit corresponds to a minimum bound on the viscosity of $\sim 2 \times 10^{19}$ Pa s. The surface deformation calculated to result from this scenario is shown in Figure 9a. If the elastic layer is taken to be thicker, the bound on the viscosity reduces, as shown in Figure 9b.

[40] In a second conceptual model of lithospheric rheology, we have assumed that the upper mantle behaves elastically (over a depth range of 25 km beneath a 35 km thick crust). Because most of the deformation occurs in the ductile lower crust in the previous model, imposing an elastic upper mantle layer does little to change the resulting viscosity bound. Observations over a longer timescale would be required to investigate where in the range of $\sim 2 \times 10^{19}$ Pa s or higher the actual viscosity lies.

[41] It is possible that long-wavelength signals could be masked by long-wavelength artifacts in the InSAR data, resulting from inaccuracies in orbital parameters. To test if these artifacts are present in our data, we have fitted E-W dipping linear planes to the ALOS displacements in each of our 60 interferograms (the variations in line-of-sight displacement expected from the viscoelastic models are largest along E-W profiles through the fault). The best-fitting planes show no consistency in dip direction (i.e. east or west), and mostly have gradients of less than 0.01 cm/km (in 51 of the 60 interferograms), which is significantly smaller than the

gradients present in the calculations that show displacements above our detection threshold of 1 cm (e.g. the ~ 0.05 cm/km shown in Figure 9a). Of the remaining interferograms, where the gradients are larger (up to 0.017 cm/km), these gradients can be seen to be dominated by features which appear to be atmospheric in origin (i.e. they are irregular in shape, rather than forming the smooth variation expected from orbital artifacts). We therefore believe that were a signal of viscoelastic relaxation present at above the level of our detection threshold (1 cm), it would not be overwhelmed by orbital artifacts, and that our estimate of $\sim 2 \times 10^{19}$ Pa s represents a true lower bound on the viscosity.

5.4. Implications for Seismic Hazard Assessment

[42] Our information regarding the faulting during the Mozambique earthquake has implications for the assessment of seismic hazard on similar fault systems. First, although the coseismic slip at the surface on the southernmost fault plane was concentrated onto a discrete fault scarp, we do not know if the postseismic afterslip also occurred on this scarp, or if it was laterally distributed over tens to hundreds of meters. If the afterslip was laterally distributed at the surface, then studies based only upon the surface fault scarp would infer an amount of total slip that was less than half of what had actually occurred in the entire seismic cycle. Additionally, studies based only upon observations of the recent motion at the surface on the northernmost fault plane would fail to capture two aspects of the deformation. First, the sense of long-term motion would be incorrectly interpreted (which from recent observations would be taken to have a significant strike-slip component, at odds with the regional strain). Secondly, the fault would be interpreted to have slipped recently. While this is true for the near-surface layers, the teleseismic data precludes significant slip at depths corresponding to the crystalline basement, where the

fault is presumably still capable of generating large earthquakes in the near future. Possibly the best way to minimize the effects of these potentially misleading observations would be to collect fault offset data spanning the largest possible numbers of timescales and distances from the fault trace.

6. Conclusions

[43] The geodetic data available for the region of the 2006 Mozambique earthquake, along with teleseismic data, have allowed us to produce a well-constrained source model and study the postseismic deformation. Where the fault cuts through the crystalline basement it behaves in a stick-slip ('velocity-weakening') manner, and has a coefficient of friction at least $\sim 25\text{--}45\%$ lower than that on optimally oriented planes. Within the sedimentary layer the fault behaved postseismically in a creeping manner ('velocity-strengthening'), although the earthquake rupture dynamically propagated into this shallow region. The presence of thick sedimentary sequences containing creeping fault zones may have a significant impact on the magnitude of the forces that can be transmitted through the seismogenic crust. The stresses generated by slip on the main fault plane of the earthquake led to significant strike-slip postseismic (and possibly coseismic) slip on the shallow part of an adjacent normal fault. Analysis of the deformation following an aftershock indicates that the value of the parameter 'a' that describes the rate-dependence of fault friction lies in the range 1×10^{-3} – 2×10^{-2} . The lack of significant long-wavelength postseismic deformation implies viscosities in the ductile lithosphere greater than $\sim 2 \times 10^{19}$ Pa s. The fault that ruptured in the earthquake had previously produced subtle features visible in the geomorphology of the region, although earthquakes similar to this one may leave misleading features in the landscape from the perspective of assessing seismic hazard.

[44] **Acknowledgments.** We thank James Jackson for help in acquiring SPOT images via ISIS/CNES. Includes material copyright CNES 2010, distribution Spot Image S.A. We thank three anonymous reviewers for helpful comments on the manuscript. We thank Pembroke College in the University of Cambridge and the Gordon and Betty Moore Foundation for financial support.

References

- Avouac, J.-P., F. Ayoub, S. Leprince, O. Konca, and D. V. Helmberger (2006), The 2005, Mw 7.6 Kashmir earthquake: Sub-pixel correlation of ASTER images and seismic waveforms analysis, *Earth Planet. Sci. Lett.*, *249*, 514–528.
- Biegel, R. L., C. G. Sammis, and J. H. Dieterich (1989), The frictional properties of simulated fault gouge having a fractal particle distribution, *J. Struct. Geol.*, *11*, 827–846.
- Biggs, J., E. A. Bergman, B. Emmerson, G. J. Funning, J. A. Jackson, B. E. Parsons, and T. J. Wright (2006), Fault identification for buried strike-slip earthquakes using InSAR: The 1994 and 2004 Al Hoceima, Morocco earthquakes, *Geophys. J. Int.*, *166*, 1347–1362.
- Bondar, I., E. A. Bergman, E. R. Engdahl, B. Kohl, Y. Kung, and K. McLaughlin (2008), A hybrid multiple event location technique to obtain ground truth event locations, *Geophys. J. Int.*, *175*, 185–201.
- Burgmann, R., D. D. Pollard, and S. J. Martel (1994), Slip distributions on faults: Effects of stress gradients, inelastic deformation, heterogeneous host-rock stiffness, and fault interaction, *J. Struct. Geol.*, *16*, 1675–1690.
- Chandrasekhar, D. V., R. Burgmann, C. D. Reddy, P. S. Sunil, and D. A. Schmidt (2009), Weak mantle in NW India probed by geodetic measurements following the 2001 Bhuj earthquake, *Earth Planet. Sci. Lett.*, *280*, 229–235.
- Chen, W., and P. Molnar (1983), Focal depths of intracontinental and intraplate earthquakes and their implications for the thermal and mechanical properties of the lithosphere, *J. Geophys. Res.*, *88*, 4183–4214.
- Copley, A., and J. Jackson (2006), Active tectonics of the Turkish-Iranian plateau, *Tectonics*, *25*, TC6006, doi:10.1029/2005TC001906.
- Copley, A., F. Boait, J. Hollingsworth, J. Jackson, and D. McKenzie (2009), Subparallel thrust and normal faulting in Albania and the role of gravitational potential energy and rheology contrasts in mountain belts, *J. Geophys. Res.*, *114*, B05407, doi:10.1029/2008JB005931.
- Copley, A., J.-P. Avouac, J. Hollingsworth, and S. Leprince (2011), The 2001 Mw 7.6 Bhuj earthquake, low fault friction, and the crustal support of plate driving forces in India, *J. Geophys. Res.*, *116*, B08405, doi:10.1029/2010JB008137.
- Craig, T. J., J. A. Jackson, K. Priestley, and D. McKenzie (2011), Earthquake distribution patterns in Africa: Their relationship to variations in lithospheric and geological structure, and their rheological implications, *Geophys. J. Int.*, *185*, 403–434.
- Dieterich, J. H., and B. D. Kilgore (1994), Direct observation of frictional contacts: New insights for state-dependent properties, *Pure Appl. Geophys.*, *143*, 283–302.
- Di Toro, G., D. L. Goldsby, and T. E. Tullis (2004), Friction falls towards zero in quartz rock as slip velocity approaches seismic rates, *Nature*, *427*, 436–439.
- Engdahl, E. R., R. van der Hilst, and R. Buland (1998), Global teleseismic earthquake relocation with improved travel times and procedures for depth determination, *Bull. Seismol. Soc. Am.*, *88*, 722–743.
- Eshelby, J. D. (1957), The determination of the elastic field of an ellipsoidal inclusion, and related problems, *Proc. R. Soc. A*, *241*, 376–396.
- Fenton, C. H., and J. J. Bommer (2006), The Mw7.3 Machaze, Mozambique, earthquake of 23 February 2006, *Seismol. Res. Lett.*, *77*, 426–439.
- Fialko, Y. (2004), Evidence of fluid-filled upper crust from observations of postseismic deformation due to the 1992 Mw7.3 Landers earthquake, *J. Geophys. Res.*, *109*, B08401, doi:10.1029/2004JB002985.
- Fialko, Y. (2009), Study of postseismic deformation due to the 2006 Mw 7.0 Mozambique (East Africa) earthquake using alos-palsar data, paper presented at 3rd ALOS PI Symposium, Kona, Hawaii, 9–13 Nov.
- Fialko, Y., D. Sandwell, M. Simons, and P. Rosen (2005), Three-dimensional deformation caused by the Bam, Iran, earthquake and the origin of shallow slip deficit, *Nature*, *435*, 295–299.
- Fielding, E. J., P. R. Lundgren, R. Burgmann, and G. J. Funning (2009), Shallow fault-zone dilatancy recovery after the 2003 Bam earthquake in Iran, *Nature*, *458*, 64–68.
- Freed, A. M., and R. Burgmann (2004), Evidence of power-law flow in the Mojave desert mantle, *Nature*, *430*, 548–551.
- Frey Mueller, J., N. E. King, and P. Segall (1994), The co-seismic slip distribution of the Landers earthquake, *J. Geophys. Res.*, *84*, 646–659.
- Goldsworthy, M., J. Jackson, and J. Haines (2002), The continuity of active fault systems in Greece, *Geophys. J. Int.*, *148*, 596–618.
- Hearn, E. H., R. Burgmann, and R. E. Reilinger (2002), Dynamics of Izmit earthquake postseismic deformation and loading of the Duzce earthquake hypocentre, *Bull. Seismol. Soc. Am.*, *92*, 172–193.
- Herman, F., et al. (2010), Exhumation, crustal deformation, and thermal structure of the Nepal Himalaya derived from the inversion of thermochronological and thermobarometric data and modeling of the topography, *J. Geophys. Res.*, *115*, B06407, doi:10.1029/2008JB006126.
- Hetenyi, G., R. Cattin, J. Vergne, and J. L. Nabelek (2006), The effective elastic thickness of the India Plate from receiver function imaging, gravity anomalies and thermomechanical modelling, *Geophys. J. Int.*, *167*, 1106–1118.
- Hsu, Y.-J., M. Simons, J.-P. Avouac, J. Galetzka, K. Sieh, M. Chlieh, D. Natawidjaja, L. Prawirodirdjo, and Y. Bock (2006), Frictional after-slip following the 2005 Nias-Simeulue earthquake, Sumatra, *Science*, *312*, 1921–1926.
- Hsu, Y.-J., S.-B. Yu, and H.-Y. Chen (2009), Coseismic and postseismic deformation associated with the 2003 Chengkung, Taiwan, earthquake, *Geophys. J. Int.*, *176*, 420–430.
- Jackson, J., D. McKenzie, K. Priestley, and B. Emmerson (2008), New views on the structure and rheology of the lithosphere, *J. Geol. Soc.*, *165*, 453–465.
- Ji, C., D. J. Wald, and D. V. Helmberger (2002), Source description of the 1999 Hector Mine, California, earthquake, part 1: Wavelet domain inversion theory and resolution analysis, *Bull. Seismol. Soc. Am.*, *92*, 1192–1207.
- Ji, C., D. V. Helmberger, D. J. Wald, and K.-F. Ma (2003), Slip history and dynamic implications of the 1999 Chi-Chi, Taiwan, earthquake, *J. Geophys. Res.*, *108*(B9), 2412, doi:10.1029/2002JB001764.
- Johanson, I. A., and R. Burgmann (2010), Coseismic and postseismic slip from the 2003 San Simeon earthquake and their effects on backthrust slip

- and the 2004 Parkfield earthquake, *J. Geophys. Res.*, *115*, B07411, doi:10.1029/2009JB006599.
- Johnson, K., R. Burgmann, and K. Larson (2006), Frictional properties on the San Andreas Fault near Parkfield, California, inferred from models of afterslip following the 2004 earthquake, *Bull. Seismol. Soc. Am.*, *96*, S321–S338, doi:10.1785/0120050808.
- Jordan, T. H., and K. A. Sverdrup (1981), Teleseismic location techniques and their application to earthquake clusters in the south-central Pacific, *Bull. Seismol. Soc. Am.*, *71*, 1105–1130.
- Kaneko, Y., and Y. Fialko (2011), Shallow slip deficit due to large strike-slip earthquakes in dynamic rupture simulations with elasto-plastic off-fault response, *Geophys. J. Int.*, *186*, 1389–1403.
- Kaneko, Y., N. Lapusta, and J.-P. Ampuero (2008), Spectral-element modeling of spontaneous earthquake rupture on rate and state faults: Effect of velocity-strengthening friction at shallow depths, *J. Geophys. Res.*, *113*, B09317, doi:10.1029/2007JB005553.
- Konca, O. (2008), Partial rupture of a locked patch of the Sumatra megathrust during the 2007 earthquake sequence, *Nature*, *456*, 631–635.
- Konca, O., S. Leprince, J.-P. Avouac, and D. V. Helmberger (2010), Rupture process of the 1999 Mw 7.1 Duzce earthquake from joint analysis of SPOT, GPS, InSAR, strong-motion, and teleseismic data: A supershear rupture with variable rupture velocity, *Bull. Seismol. Soc. Am.*, *100*, 267–288.
- Kositsky, A. P., and J.-P. Avouac (2010), Inverting geodetic time series with a principal component analysis-based inversion method, *J. Geophys. Res.*, *115*, B03401, doi:10.1029/2009JB006535.
- Lamb, S. (2006), Shear stresses on megathrusts: Implications for mountain building behind subduction zones, *J. Geophys. Res.*, *111*, B07401, doi:10.1029/2005JB003916.
- Langbein, J., A. McGarr, J. S. Johnston, and P. W. Harsh (1983), Geodetic measurements of postseismic crustal deformation following the 1979 Imperial Valley earthquake, California, *Bull. Seismol. Soc. Am.*, *73*, 1203–1224.
- Lapusta, N., and J. R. Rice (2003), Low-heat and low-stress fault operation in earthquake models of statically strong but dynamically weak faults, *In Eos Trans. AGU 84(46)*, Fall Meet. Suppl., Abstract S51B-02.
- Leprince, S., S. Barbot, F. Ayoub, and J.-P. Avouac (2007), Automatic and precise ortho-rectification, coregistration, and subpixel correlation of satellite images, application to ground deformation measurements, *IEEE Trans. Geosci. Remote Sens.*, *45*, 1529–1558.
- Leprince, S., P. Muse, and J.-P. Avouac (2008), In-flight CCD distortion calibration for pushbroom satellites based on subpixel correlation, *IEEE Trans. Geosci. Remote Sens.*, *46*, 2675–2683.
- Marone, C. J., C. B. Raleigh, and C. H. Scholz (1990), Frictional behavior and constitutive modeling of simulated fault gouge, *J. Geophys. Res.*, *95*, 7007–7025.
- Marone, C. J., C. H. Scholtz, and R. Bilham (1991), On the mechanics of earthquake afterslip, *J. Geophys. Res.*, *96*, 8441–8452.
- Nissen, E., F. Yamini-Fard, M. Tatar, A. Gholamzadeh, E. Bergman, J. R. Elliott, J. A. Jackson, and B. Parsons (2010), The vertical separation of mainshock rupture and microseismicity at Qeshm island in the Zagros fold-and-thrust belt, Iran, *Earth Planet. Sci. Lett.*, *296*, 181–194.
- Nissen, E., M. Tatar, J. A. Jackson, and M. B. Allen (2011), New views on earthquake faulting in the Zagros fold-and-thrust belt of Iran, *Geophys. J. Int.*, *186*, 928–944.
- Nocquet, J.-M., P. Willis, and S. Garcia (2006), Plate kinematics of Nubia-Somalia using combined DORIS and GPS solution, *J. Geod.*, *80*, 591–607.
- Perfettini, H., and J.-P. Avouac (2004), Postseismic relaxation driven by brittle creep: A possible mechanism to reconcile geodetic measurements and the decay rate of aftershocks, application to the Chi-Chi earthquake, Taiwan, *J. Geophys. Res.*, *109*, B02304, doi:10.1029/2003JB002488.
- Perfettini, H., and J.-P. Avouac (2007), Modeling afterslip and aftershocks following the 1992 Landers earthquake, *J. Geophys. Res.*, *112*, B07409, doi:10.1029/2006JB004399.
- Pollitz, F. F. (1992), Postseismic relaxation theory on the spherical Earth, *Bull. Seismol. Soc. Am.*, *82*, 422–453.
- Raucoules, D., B. Ristori, M. de Michele, and P. Briole (2010), Surface displacement of the Mw 7 Machaze earthquake (Mozambique): Complementary use of multiband InSAR and radar amplitude image correlation with elastic modelling, *Remote Sens. Environ.*, *114*, 2211–2218.
- Rice, J. R. (1993), Spatio-temporal complexity of slip on a fault, *J. Geophys. Res.*, *98*, 9885–9907.
- Rosen, P. A., S. Hensley, and G. Peltzer (2004), Updates repeat orbit interferometry package released, *Eos Trans. AGU*, *85(5)*, 47, doi:10.1029/2004EO050004.
- Salman, G., and I. Abdula (1995), Development of the Mozambique and Rovuma sedimentary basins, offshore Mozambique, *Sediment. Geol.*, *96*, 7–41.
- Savage, J. C., and W. H. Prescott (1978), Asthenosphere readjustment and the earthquake cycle, *J. Geophys. Res.*, *83*, 3369–3376.
- Smith, W. H. F., and P. Wessel (1990), Gridding with continuous curvature splines in tension, *Geophysics*, *55*, 293–305.
- Townend, J., and M. D. Zoback (2000), How faulting keeps the crust strong, *Geology*, *28*, 399–402.
- Watts, A. B. (2001), Gravity anomalies, flexure, and crustal structure at the Mozambique rifted margin, *Mar. Pet. Geol.*, *18*, 445–455.
- Watts, A. B., and E. B. Burov (2003), Lithospheric strength and its relationship to the elastic and seismogenic layer thickness, *Earth Planet. Sci. Lett.*, *213*, 113–131.
- Yang, Z., and W.-P. Chen (2008), Mozambique earthquake sequence of 2006: High-angle normal faulting in southern Africa, *J. Geophys. Res.*, *113*, B12303, doi:10.1029/2007JB005419.

E. Bergman, Global Seismological Services, 1900 19th St., Golden, CO 80401, USA.

A. Copley, COMET+, Bullard Labs, Department of Earth Sciences, University of Cambridge, Cambridge CB3 0EZ, UK. (acc41@cam.ac.uk)

J. Hollingsworth, Tectonics Observatory, Division of Geological and Planetary Sciences, California Institute of Technology, Pasadena, CA 91125, USA.